Environmental Science and Pollution Research (2023) 30:49301–49313
https://doi.org/10.1007/s11356-023-25678-2

RESEARCH ARTICLE

Adsorption of nitrophenol onto a novel Fe_3O_4-κ-carrageenan/MIL-125(Ti) composite: process optimization, isotherms, kinetics, and mechanism

Eman M. Abd El-Monaem[1] · Abdelazeem S. Eltaweil[1] · Gehan M. El-Subruiti[1] · Mohamed S. Mohy-Eldin[2] · Ahmed M. Omer[2]

Received: 17 September 2022 / Accepted: 29 January 2023 / Published online: 11 February 2023

Abstract

Water pollution is a dreadful affair that has incessantly aggravated, exposing our planet to danger. In particular, the persistent nitro aromatic compound like nitrophenols causes anxiety to the researchers due to their hazardous impacts, excessive usage, and removal difficulty. For this purpose, a novel multi-featured composite was constructed based on κ-Carrageenan (κ-Carr), MOF (MIL-125(Ti)), and magnetic Fe_3O_4 for efficient adsorptive removal of o-nitrophenol (o-NP). Interestingly, BET measurements revealed the high surface area of Fe_3O_4-κ-Carr/MIL-125(Ti) of about 163.27 m^2/g, while VSM showed its excellent magnetic property (20.34 emu/g). The comparison study pointed out the synergistic effect between Fe_3O_4, κ-Carr, and MIL-125(Ti), forming a composite with an excellent adsorption performance toward o-NP. The adsorption data obeyed pseudo-second-order kinetic model, and Freundlich isotherm model was better fitted than Langmuir and Temkin. Furthermore, Langmuir verified the supreme adsorption capacity of o-NP onto Fe_3O_4-κ-Carr/MIL-125(Ti) since the computed q_{max} reached 320.26 mg/g at pH 6 and 25 °C. Furthermore, the XPS results postulated that the adsorption mechanism pf o-NP proceeded via H-bonding, π-π interaction, and electron donor–acceptor interactions. Interestingly, Fe_3O_4-κ-Carr/MIL-125(Ti) composite retained good adsorption characteristics after reusing for five cycles, suggesting its viable applicability as an efficient, renewable, and easy-separable adsorbent for removing nitro aromatic pollutants.

Keywords κ-Carrageenan · MOF (MIL-125(Ti)) · Magnetic composite · Nitrophenol · Adsorption · Reusability

Introduction

Water pollution by the fatal aromatic compounds is swiftly exacerbated, threatening humanity's existence (Das et al. 2021; Kassem et al. 2021; Priyadarshi et al. 2022). Nitrophenol is one of the most pernicious aromatic compounds since it is widely applied in diversified industries such as dyes, insecticides, medicines, and petrochemicals (Abdelfatah et al. 2021a; Liu et al. 2020). Consequently, colossal amounts of nitrophenol have been disposed into waterbodies, causing deleterious impacts on human health, such as damage to kidneys and liver, blurred vision, systemic poisoning, and mouth irritation (Benmaati et al. 2022; Ma et al. 2019). In addition to the dangerous effects on the environment, the presence of the nitro group in nitrophenol enhances its stability in soil and water bodies (Ewis et al. 2022). Hence, several remediation techniques have been fostered to get rid of these detrimental contaminants from water bodies, such as membrane separation, coagulation, electrolysis, ion exchange, and adsorption (Abdelfatah et al. 2021a, Abdelfatah et al. 2021b, Eltaweil et al. 2022a, Karim et al. 2019, Li et al. 2021, Sadoon and M-Ridha 2019, Saha et al. 2022, Tran et al. 2021, Wu et al. 2021). The former technique has been applied more widely than the other techniques owing to its simplicity, low cost, high-efficacy,

Responsible Editor: Tito Roberto Cadaval Jr

✉ Eman M. Abd El-Monaem
emanabdelmonaem5925@yahoo.com

[1] Chemistry Department, Faculty of Science, Alexandria University, Alexandria, Egypt

[2] Polymer Materials Research Department, Advanced Technology and New Materials Research Institute (ATNMRI), City of Scientific Research and Technological Applications (SRTA-City), P. O. Box: 21934, New Borg El-Arab City, Alexandria, Egypt

and low-energy consumption (Abdelfatah et al. 2022; Deb et al. 2021; Gomaa et al. 2022b; Mokhtar et al. 2020; Raval et al. 2021; Zhao et al. 2021).

Carrageenan is an anionic polysaccharide polymer extracted from red seaweed (Yu et al. 2019). Carrageenan involves sulfate groups, and it is classified into theta, beta, iota, lambda, alpha, and kappa based on the position and numbers of the attached sulfate groups onto the carrageenan skeleton (Sharma et al. 2022). Interestingly, κ-Carr is vastly utilized in the food industries since it has remarkable thickening, stabilizing, and gelling properties (Ammar et al. 2021). Furthermore, the eco-friendly, availability, biodegradability, and biocompatibility characteristics of κ-Carr render it a promising adsorbent for removing contaminants (Li et al. 2019). In spite of the remarkable advantages of κ-Carr, it still suffers some limitations, including an inferior gel strength and poor environmental stability (Lapwanit et al. 2018). Thence, several attempts have been implemented to overcome these flaws, including modification of κ-Carr with carbon materials, magnetic nanoparticles, zeolite, and other polymers (Duman et al. 2019, 2016; Huang et al. 2022; Mittal et al. 2020). Notably, it was reported an enhancement in the κ-Carr properties by impregnating metal–organic frameworks (MOFs) into its matrix (Klongklaew and Bunkoed 2021). Nevertheless, there is a scarcity of research papers that involves the fabrication of κ-Carr/MOF composites.

Strikingly, the applications of MOFs have been raised day-by-day in diversified fields such as drug delivery, solar cell, gas storage, batteries, and especially in water remediation. (Lazaro and Forgan 2019, Shen et al. 2021; Xu et al. 2022). Due to their excellent chemical and thermal stability, high surface area, porous structure, water stability, and ease of functionalization, MOFs have gained vast concern as propitious adsorbents (Abd El-Monaem et al. 2022). Titanium-based MIL-125 is a shining member of the remarkable MIL family that possesses excellent adsorption performance owing to excellent chemical stability, redox potential, and thermal stability (Fatima et al. 2020). Interestingly, MIL-125(Ti) has revealed an enhanced adsorption performance toward pharmaceutical residues, organic dyes, and heavy metals (Jiang et al. 2021; Liang et al. 2018; Liu et al. 2021; Omer et al. 2021). However, the difficult separation of MIL-125(Ti) after the adsorption process with the traditional techniques is a big obstacle. To overcome this disadvantage, incorporating magnetic nanoparticles in the adsorbent matrix enable easy separation of them after adsorption. One of the most extensively utilized magnetic nanoparticles is magnetite due to its ease of synthesis, biocompatibility, high surface area, and abundant active sites (Attia et al. 2022; Toto et al. 2022). Despite the construction of various composites from MIL-125(Ti) with many polysaccharides, there are no study reported the fabrication of MIL-125(Ti)/κ-Carr composite and the evaluation of its adsorbability toward organic pollutants or any other water contaminants.

Herein, we adopted a developed avenue to foster the adsorption performance of κ-Carr through its combination with MIL-125(Ti). Furthermore, to overcome the separation difficulty, κ-Carr/MIL-125(Ti) composite was decorated by magnetic nanoparticles (Fe_3O_4). Assorted characterization tools were utilized to infer the successful fabrication of Fe_3O_4-κ-Carr/MIL-125(Ti) and study its chemical and physical properties. The adsorbability of Fe_3O_4-κ-Carr/MIL-125(Ti) composite was examined in the adsorption of o-nitrophenol (o-NP) from an aqueous solution. Besides, the reusability of Fe_3O_4-κ-Carr/MIL-125(Ti) composite was confirmed by executing the recyclability test for five cycles. More importantly, the mechanism of the o-NP adsorption onto Fe_3O_4-κ-Carr/MIL-125(Ti) composite was understood thoroughly based on XPS results.

Experimental part

Materials

Ferrous chloride tetrahydrate ($FeCl_2.4H_2O$), glutaraldehyde, and ethanol were supplied from Aladdin Industrial Corporation, China. Ammonium solution (NH_4OH), 1,4-benzene dicarboxylic acid (BDC), and N,N dimethyl formamide (DMF) were purchased from Sinopharm Chemical Reagent, China. κ-Carrageenan, ferric chloride hexahydrate ($FeCl_3.6H_2O$), o-nitrophenol, and titanium tetraisoproproxide ($Ti(O\text{-}iPr)_4$) were provided from Sigma-Aldrich, USA.

Fabrication of Fe_3O_4 nanoparticles

Fe_3O_4 was prepared as reported in the author's previous study (Eltaweil et al. 2021). Under the N_2 atmosphere, the specific amounts of $FeCl_3.6H_2O$ and $FeCl_2.4H_2O$ were dissolved into 500 mL double-distilled water. Then, ammonium solution was dropped slowly into the Fe^{2+}/Fe^{3+} solution until pH reached 10. The resultant solution was stirred at 80 °C for 9 min. Finally, the obtained Fe_3O_4 particles were collected via a magnet, washed, and dried at 70 °C.

Fabrication of MIL-125(Ti)

MIL-125(Ti) was prepared as follows: 995 mg BDC was dissolved into 25 mL DMF under magnetic stirring for 15 min. Then, 1.35 mL $Ti(O\text{-}iPr)_4$ was dipped into the BDC solution and kept under vigorous stirring for 1 h. Next, Ti/BDC

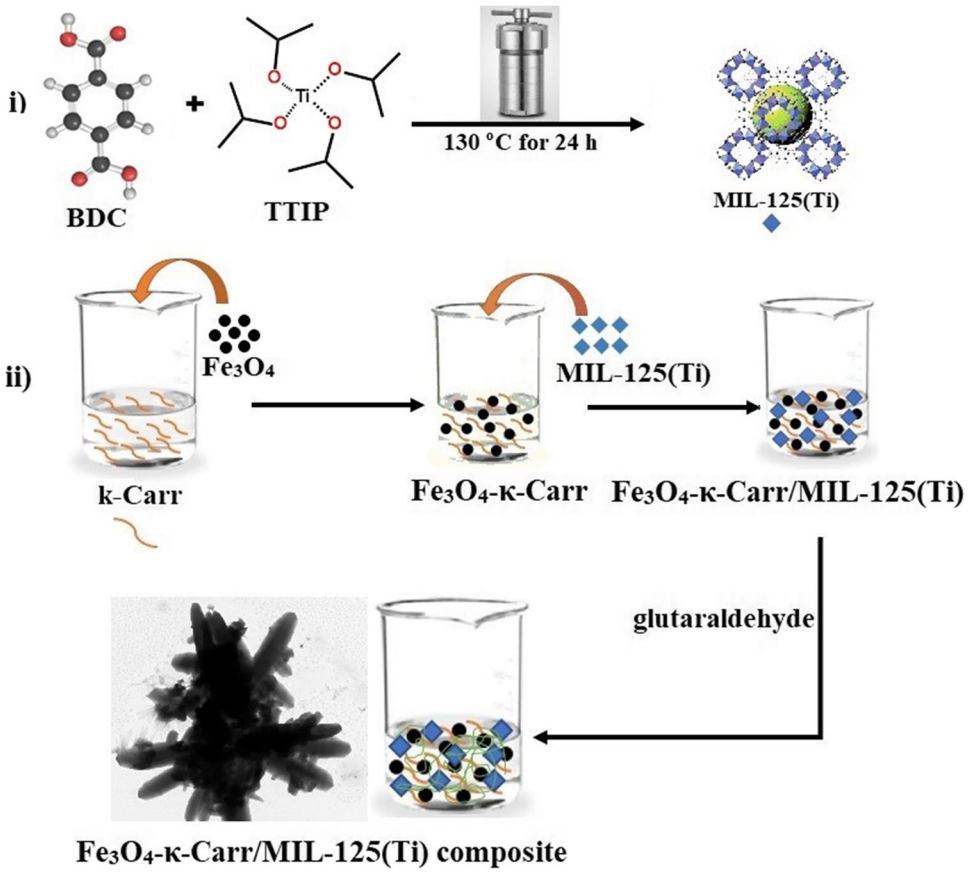

Scheme 1 The preparation method of Fe_3O_4-κ-Carr/MIL-125(Ti)

solution was poured into a 100 mL autoclave and heated at 130 °C for 24 h. Ultimately, the obtained solid was collected by centrifugation, washed, and dried at 80 °C for 24 h (Yang et al. 2018).

Fabrication of Fe_3O_4-κ-Carr/MIL-125(Ti) composite

Fe_3O_4-κ-Carr/MIL-125(Ti) composite was prepared as follows: a particular amount of κ-Carr was dissolved into 25 mL dist. H_2O at 70 °C. Then, 0.02 g Fe_3O_4 was dipped into κ-Carr solution and kept under stirring for 1 h, allowing the magnetic nanoparticles to diffuse into κ-Carr layers. MIL-125(Ti) was added bit-by-bit to Fe_3O_4/κ-Carr composite under vigorous stirring, followed by adding 6 mL of glutaraldehyde. After 1 h, Fe_3O_4-κ-Carr/MIL-125(Ti) composite was collected, washed, and dried at 50 °C for 24 h. Fe_3O_4-κ-Carr/MIL-125(Ti) composite was prepared with three mass ratios of κ-Carr/MIL-125(Ti) = 1:1, 1:3, and 3:1 (Scheme 1).

Characterization

Fe_3O_4-κ-Carr/MIL-125(Ti) composite and its components were characterized by Fourier transform infrared spectra (FTIR; NEXUS-670), Brunauer–Emmett–Teller method (BET; Tristar II 3020), X-ray diffractometer (XRD; MAC Science M03XHF), zeta potential (ZP; Malvern-UK), X-ray photoelectron spectroscopy (XPS; Escalab 250Xi), vibrating-sample magnetometer (VSM; Lakeshore), scanning electron microscope (SEM; Hitachi-S4800), and transmission electron microscope (TEM; JOEL, 110 kV).

Batch adsorption

The optimum conditions to adsorb o-NP onto Fe_3O_4-κ-Carr/MIL-125(Ti) composite were defined in a batch mode. A series of the o-NP adsorption process proceeded at a pH range from 2 to 10 to identify the optimum pH. Furthermore, the impact of the Fe_3O_4-κ-Carr/MIL-125(Ti) dose on the adsorption aptitude of o-NP was determined at a dose range from 0.005 to 0.02 g. Moreover, the influence of the temperature on the removal efficiency of o-NP was examined at a temperature range from 25 to 55 °C. Finally, the impact of the initial concentration of o-NP was studied at a concentration range from 50 to 200 mg/L. The residual concentration of o-NP was measured according to the standard methods to examine water and wastewater (Rice et al. 2012) using UV–Vis spectrophotometer (PG 82 +, UK) at 344 nm, then the adsorption capacity and the removal % of o-NP were calculated by the following equations:

$$R\% = \frac{C_0 - C_t}{C_0} \times 100 \quad (1)$$

$$q_e = \frac{(C_0 - C_t) \times V}{m} \quad (2)$$

where C_0 and C_t symbolize the initial concentration of o-NP and the concentration at time t, respectively. m and V symbolize the mass of Fe_3O_4-κ-Carr/MIL-125(Ti) and the volume of o-NP solution, respectively.

Recyclability test

To evaluate the regeneration potential of Fe_3O_4-κ-Carr/MIL-125(Ti) composite, the used composite was separated after the o-NP adsorption and subsequently soaked into 25 mL 1 M NaOH under magnetic stirring to desorb o-NP from its surface. Then, the recycled composite was washed with distilled H_2O and utilized in the next cycle, repeating this adsorption/desorption cycle five times.

Ionic strength test

The influence of the ionic strength on the o-NP adsorption aptitude was assessed as follows: a specific weight of NaCl (0.2–1.0 mol/L) was soaked in 20 mL of o-NP at pH 6. Then, 10 mg of Fe_3O_4-κ-Carr/MIL-125(Ti) was added to o-NP/NaCl solution under stirring. After 60 min, a sample was withdrawn and measured to determine the concentration of the un-adsorbed o-NP.

Results and discussion

Characterization of Fe_3O_4-κ-Carr/MIL-125(Ti) composite

Morphology study

SEM was utilized to identify the morphology of the as-synthesized Fe_3O_4-κ-Carr/MIL-125(Ti) composite and its pure components. The SEM image of κ-Carr (Fig. 1A) reveals its fiber-like morphology with a smooth surface, while the SEM image (Fig. 1B) showed the aggregated spherical particles of Fe_3O_4 in nanosize. Such aggregation is most likely due to the magnetic nature of Fe_3O_4. Furthermore, the SEM image of MIL-125(Ti) depicts a quasi-spherical morphology with irregular size (Fig. 1C). SEM of Fe_3O_4-κ-Carr/MIL-125(Ti) composite suggested the incorporation of Fe_3O_4 and MIL-125(Ti) particles into κ-Carr (Fig. 1D).

The TEM image (Fig. 1E) exhibited the quasi-spherical morphology of Fe_3O_4 with an average particle size of about 19.71 nm. In addition, the image revealed an aggregation of Fe_3O_4 particles owing to their magnetic nature. The TEM image of Fe_3O_4-κ-Carr/MIL-125(Ti) composite (Fig. 1F) showed the distributed particles of Fe_3O_4 and MIL-125(Ti)

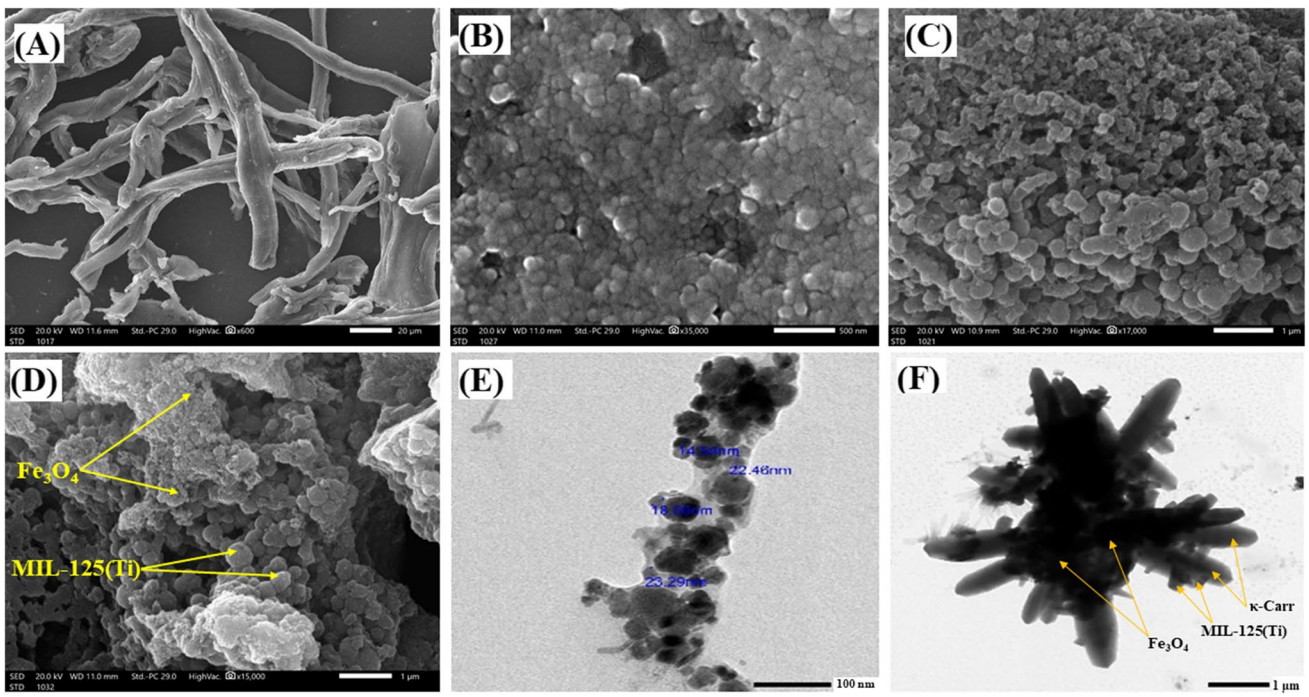

Fig. 1 SEM images of **A** κ-Carr, **B** Fe_3O_4, **C** MIL-125(Ti), and **D** Fe_3O_4-κ-Carr/MIL-125(Ti) and TEM images of **E** Fe_3O_4 and **F** Fe_3O_4-κ-Carr/MIL-125(Ti)

onto the fiber-like particles of κ-Carr, denoting the successful combination between the composite's components.

XRD

The crystallite phases of Fe_3O_4, κ-Carr, MIL-125(Ti), and Fe_3O_4-κ-Carr/MIL-125(Ti) composite were analyzed by XRD (Fig. 2A). The XRD pattern of κ-Carr signalizes its characteristic broad band around $2\theta = 20°$ (Rhim and Wang 2014). Moreover, the XRD pattern of Fe_3O_4 elucidates its discriminative peaks at $2\theta = 30.01$, 35.92, 42.48, 57.20, and 62.08° which are corresponded to (220), (311), (400), (511), and (440), respectively (Loh et al. 2008). The XRD pattern reveals the crystalline structure of MIL-125(Ti) since the distinguishing peaks appeared at $2\theta = 7.11$, 10.17, 12.51, 14.53, 16.51, 17.77, 24.57, 26.49, 29.49. 31.79, 34.13, 36.29, 39.49, 47.53, 56.39, and 62.71° (Omer et al. 2021). The XRD pattern of Fe_3O_4-κ-Carr/MIL-125(Ti) composite illustrates the characteristic peaks to the pure components but with a diminution in the crystallinity which is most likely due to the amorphous character of κ-Carr.

FTIR

Figure 2B depicts the FTIR spectra of κ-Carr, Fe_3O_4, MIL-125, and Fe_3O_4-κ-Carr/MIL-125(Ti) composite. For κ-Carr, the peaks at 847 and 1260 cm^{-1} are assigned to C-O-S and O = S = O, respectively (Khoshkho et al. 2021). In addition to the peak belonging to C–O–C in 3, 6-anhydrogalactose appeared at 928 cm^{-1} (Arof et al. 2010). The peaks at 1071 and 1128 cm^{-1} are ascribed to S–O and C-O, respectively. While the related peaks of OH and C-H appeared at 3435 and 2909 cm^{-1}, respectively (Khoshkho et al. 2021). For pristine Fe_3O_4, the characteristic peaks of Fe–O stretching manifested at 557 and 1405 cm^{-1}. In addition, the absorption peaks at 892 and 1639 cm^{-1} are ascribed to OH vibrating and OH bending modes, respectively, while the band at 3437 cm^{-1} belongs to OH stretching vibration (Cheng et al. 2021). For MIL-125(Ti), the sharp absorbance peak at 1398 cm^{-1} corresponds to OH of BDC. Furthermore, the characteristic peaks of symmetric C = O of BDC appeared at 1398 cm^{-1} and the asymmetric C = O manifested at 1509 and 1564 cm^{-1} (Jin et al. 2015). In addition, the peaks between 1400 and 1600 cm^{-1} are ascribed to COO of BDC, and the peak at 749 cm^{-1} is attributed to Ti–O (Moreira et al. 2018; Omer et al. 2021). For Fe_3O_4-κ-Carr/MIL-125(Ti) composite, the FTIR spectrum reveals the discriminative peaks of κ-Carr, Fe_3O_4, and MIL-125(Ti) with slight peaks shifting and lower peaks intensity, suggesting the successful combination between the pure components.

XPS

XPS spectra inferred the incorporation of MIL-125(Ti) and Fe_3O_4 into the Carr matrix. The XPS survey (Fig. 3A) implied that Fe_3O_4-κ-Carr/MIL-125(Ti) composite consists from C1s, Ti2p, Fe2p, S2p, and O1s. The C1s-spectrum (Fig. 3B) signalized the characteristic peaks of C-O, C–C, and O-C = O at 286.32, 284.52, and 288.59 eV, respectively (Cheng et al. 2022). Moreover, the Ti2p-spectrum (Fig. 3C) illustrated the peaks at 464.12, 470.94, and 458.50 eV which are corresponded to $Ti^{4+}2p1/2$, satellite, and $Ti^{4+}2p3/2$, respectively. The Fe2p-spectrum (Fig. 3D) revealed the presence of Fe^{2+} and Fe^{3+} since the distinguishing peaks to Fe^{2+} appeared at 710.55 and 727.09 eV, while the belonging peaks to Fe^{3+} manifested at 713.50 and 732.28 eV. Furthermore, the related peaks to SO_4^{2-} group of Carr appeared at 168.83 and 170.10 eV (Fig. 3E). The O1s-spectrum (Fig. 3F) showed the containing oxygen-functionalized groups onto the Fe_3O_4-κ-Carr/MIL-125(Ti) backbone since the peaks at 532.80, 531.42, and 529.66 eV are assigned to SO_4^{2-}, Fe–O/Ti–O, and C-O, respectively.

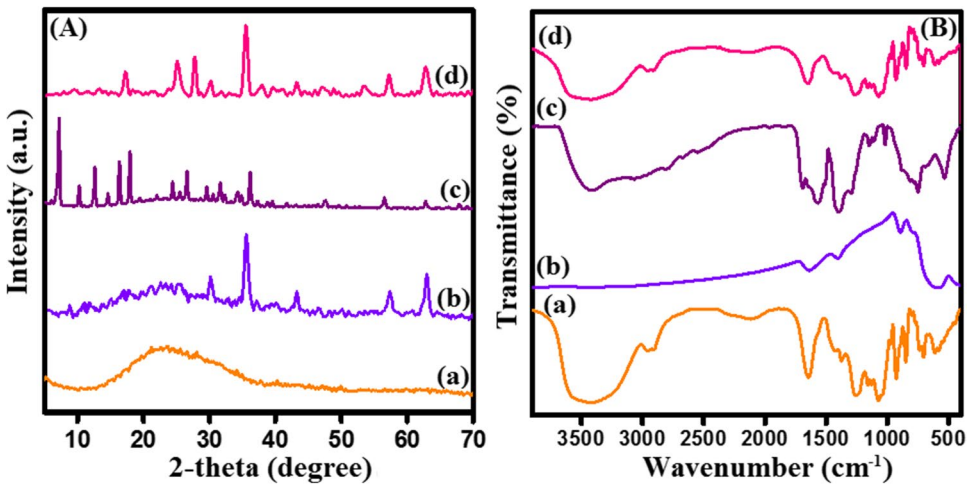

Fig. 2 **A** XRD and **B** FTIR of (a) κ-Carr, (b) Fe_3O_4, (c) MIL-125, and (d) Fe3O4-κ-Carr/MIL-125(Ti)

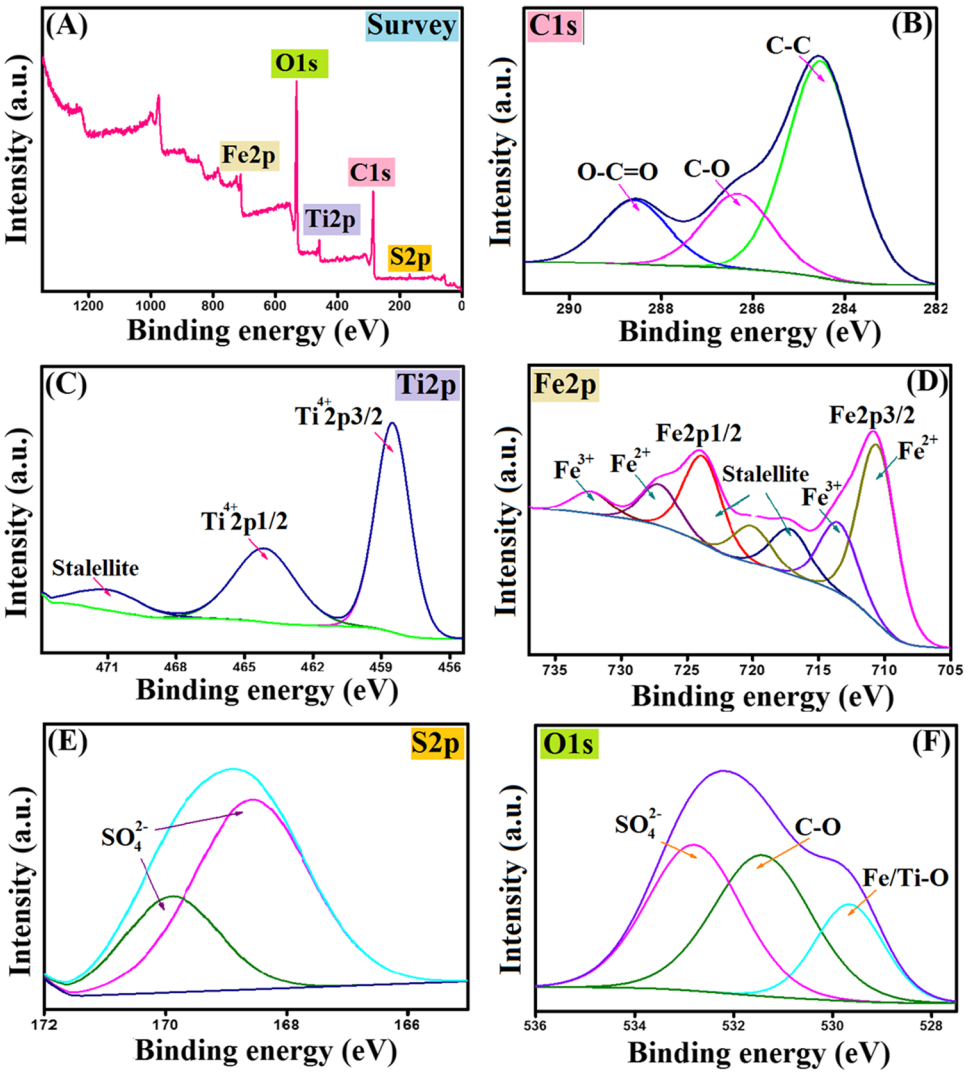

Fig. 3 XPS spectra of Fe_3O_4-κ-Carr/MIL-125(Ti). **A** Survey, **B** C1s, **C** Ti2p, **D** Fe2p, **E** S2p, and **F** O1s

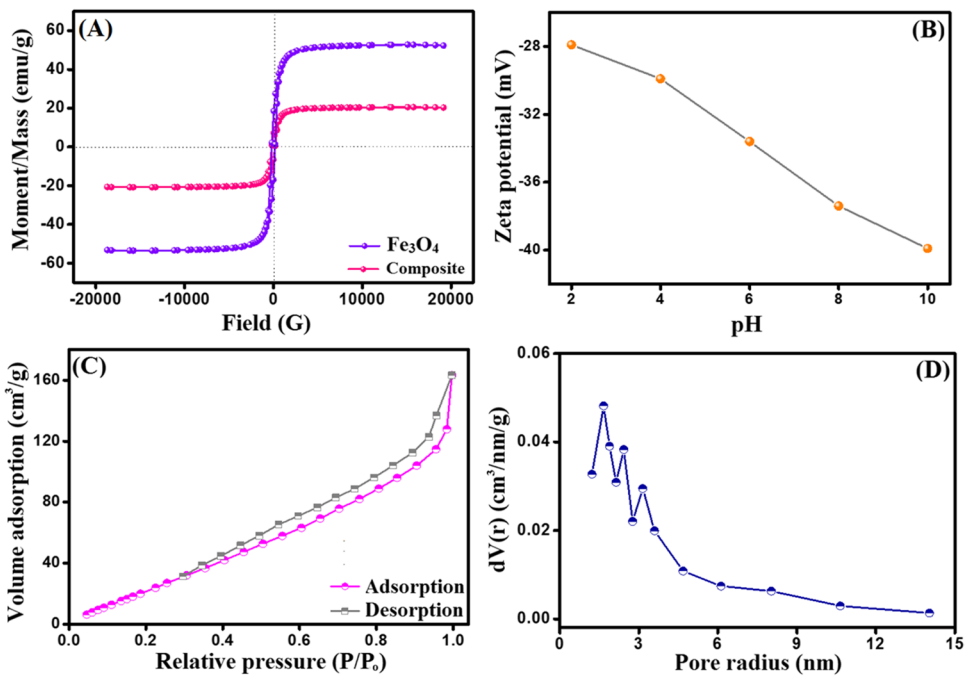

Fig. 4 **A** VSM of Fe_3O_4 and Fe_3O_4-κ-Carr/MIL-125(Ti), **B** ZP of Fe_3O_4-κ-Carr/MIL-125(Ti), **C** N_2-adsorption/desorption isotherm, and **D** the pore size distribution of Fe_3O_4-κ-Carr/MIL-125(Ti)

VSM

VSM hysteresis loops (Fig. 4A) confirmed the ferromagnetic property of both Fe_3O_4 and Fe_3O_4-κ-Carr/MIL-125(Ti) composite since the coercivity values were 199.86 and 94.56 G, respectively. Moreover, an expected decline in the saturation magnetization of Fe_3O_4 (Ms = 52.34 emu/g) occurred which is most likely due to its blinding with the non-magnetic Carr and MIL-125(Ti). Notably, Fe_3O_4-κ-Carr/MIL-125(Ti) composite possesses a propitious magnetic property (Ms = 20.34 emu/g), endowing it the easy separation advantage by an external magnet instead of the conventional techniques that consume a long time.

ZP measurements

Figure 4B depicts the ZP measurements of Fe_3O_4-κ-Carr/MIL-125(Ti) composite at a pH ranging from 3 to 11. It is apparent that Fe_3O_4-κ-Carr/MIL-125(Ti) composite displayed a negatively charged surface, while the ZP value was amplified from − 27.9 to − 39.9 mV with a raising of the pH from 2 to 10, respectively. This finding suggests the suitability of Fe_3O_4-κ-Carr/MIL-125(Ti) to adsorb zwitter ionic, neutral, and cationic pollutants.

BET

The N_2-adsorption/desorption isotherm (Fig. 4C) elucidated that Fe_3O_4-κ-Carr/MIL-125(Ti) composite showed a type II with H_4-type hysteresis loop according to the IUPAC classification, suggesting the mesoporous structure of the composite. Moreover, the specific surface area of Fe_3O_4-κ-Carr/MIL-125(Ti) composite was 163.27 m^2/g, and the average pore diameter was 2.861 nm (Fig. 4D).

Optimization of the o-NP adsorption process

Comparison test

For assessing the amelioration of the adsorption performance of Carr toward o-NP after blinding with MIL-125(Ti), a comparison test was executed between the pure materials and the three fabricated composites (Fig. 5A). It was found that the removal % of Fe_3O_4, κ-Carr, and MIL-125(Ti) were 17.35, 28.35, and 49.55% and the adsorption capacity were 22.86, 33.12, and 52.91 mg/g, respectively. Furthermore, the removal % and the adsorption capacity of Fe_3O_4-κ-Carr/MIL-125(Ti) composites with κ-Carr: MIL-125(Ti) ratios 3:1, 1:1, and 1:3 were 60.99, 65.19, and 77.55% and 63.60, 67.51, and 79.05 mg/g, respectively (Table S1). In light of these results, the modification of κ-Carr with efficient material like MIL-125(Ti) is an effective approach as it increased the removal % of o-NP by more than 2.5-fold. In addition to the dual function of Fe_3O_4 that provides perfect separation and enhances the adsorption aptitude of o-NP, the Fe_3O_4-κ-Carr/MIL-125(Ti) composite with a ratio of 1:3 between κ-Carr and MIL-125(Ti) was chosen for the rest of the batch experiments.

Effect of the solution pH

In general, pH is the dominant parameter in the uptake processes, so the o-NP uptake onto Fe_3O_4-κ-Carr/MIL-125(Ti) composite was investigated at a wide scale of pH media

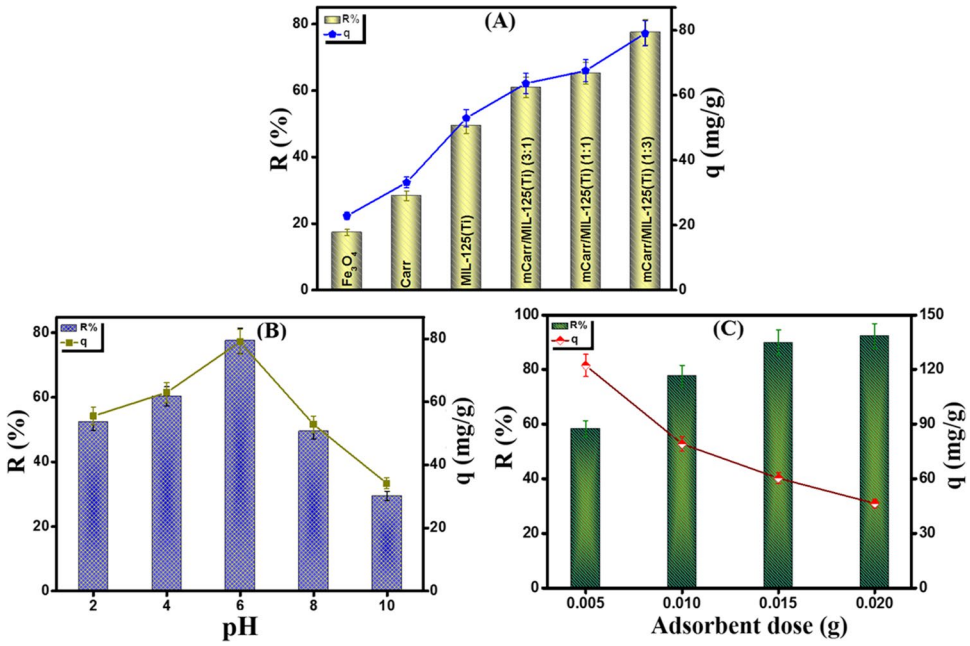

Fig. 5 **A** Comparison study [pH = 6, C_o = 50 mg/L, m = 0.01 g, and T = 25 °C], **B** the impact of pH medium [pH = 2–10, C_o = 50 mg/L, m = 0.01 g, and T = 25 °C], and **C** the impact of the Fe_3O_4-κ-Carr/MIL-125(Ti) dose [m = 0.005–0.02 g, C_o = 50 mg/L, pH = 6, and T = 25 °C] on the o-NP adsorption

(Fig. 5B). The experimental results indicated the superiority of the o-NP adsorption onto Fe_3O_4-κ-Carr/MIL-125(Ti) at pH 6. This finding could be explained by the pKa of o-NP = 7.23, meaning that o-NP exists in the molecular form in acidic conditions (Ma et al. 2019; Marques et al. 2020). Thereby, the electrostatic interaction is not the controlling mechanism on the adsorption of o-NP onto Fe_3O_4-κ-Carr/MIL-125(Ti), and there are other chemical and physical interactions such as π-π interaction, H-bonding, and electron donor–acceptor interaction could take place between o-NP and Fe_3O_4-κ-Carr/MIL-125(Ti) in the acidic medium (Chen et al. 2017). Conversely, it was observed a dramatic diminution in the o-NP adsorption aptitude when pH > 6 since the removal % and the adsorption capacity of o-NP dwindled from 77.55% and 79.05 mg/g to 26.02% and 34.18 mg/g. This finding may be anticipated by the strong repulsion forces between the anionic o-NP and the negatively charged Fe_3O_4-κ-Carr/MIL-125(Ti) composite (Liu et al. 2020).

The effect of the adsorbent dose

Figure 5C represents the impact of the dosage of Fe_3O_4-κ-Carr/MIL-125(Ti) composite onto the adsorption efficiency o-NP. It is apparent that the augmentation in the composite dose from 0.005 to 0.02 g causes an increase in the removal % of o-NP from 58.28 to 92.29%, respectively, which is most likely due to the increase in the number of active sites. On the contrary, a decline in the adsorption capacity of o-NP from 122.12 to 46.40 mg/g was observed with the raising in the Fe_3O_4-κ-Carr/MIL-125(Ti) dose which may be attributed to the aggregation of the extra amount of the composite, resulting in a diminution in the surface area.

The effect of ionic strength

Figure 6A reveals the impact of the ionic strength on the o-NP adsorption onto Fe_3O_4-κ-Carr/MIL-125(Ti) composite. It was recorded an enhancement in the adsorption aptitude of o-NP with the increase in the NaCl concentration from 0.2 to 1.0 mol/L since the adsorption capacity and removal % incremented from 79.31% and 81.33 mg/g to 87.93% and 92.45 mg/g, respectively. This behavior is most likely due to the salting out effect as the presence of NaCl declines the o-NP solubility, agreeing with Mengzhi Yang et al. 2018 (Yang and Wang 2018).

The effect of the temperature

It was deduced the exothermal nature of the o-NP adsorption onto Fe_3O_4-κ-Carr/MIL-125(Ti) since the adsorption capacity and removal % of o-NP dwindled from 79.05 mg/g and 77.55% to 65.82 mg/g and 63.38% with raising the process temperature from 25 to 55 °C, respectively (Fig. 6B). This behavior may be assigned to the increase in the system temperature causes an increment in the Brownian motion of the o-NP molecules inside the bulk solution. Hence, the adsorption aptitude o-NP onto the Fe_3O_4-κ-Carr/MIL-125(Ti) surface directly diminished.

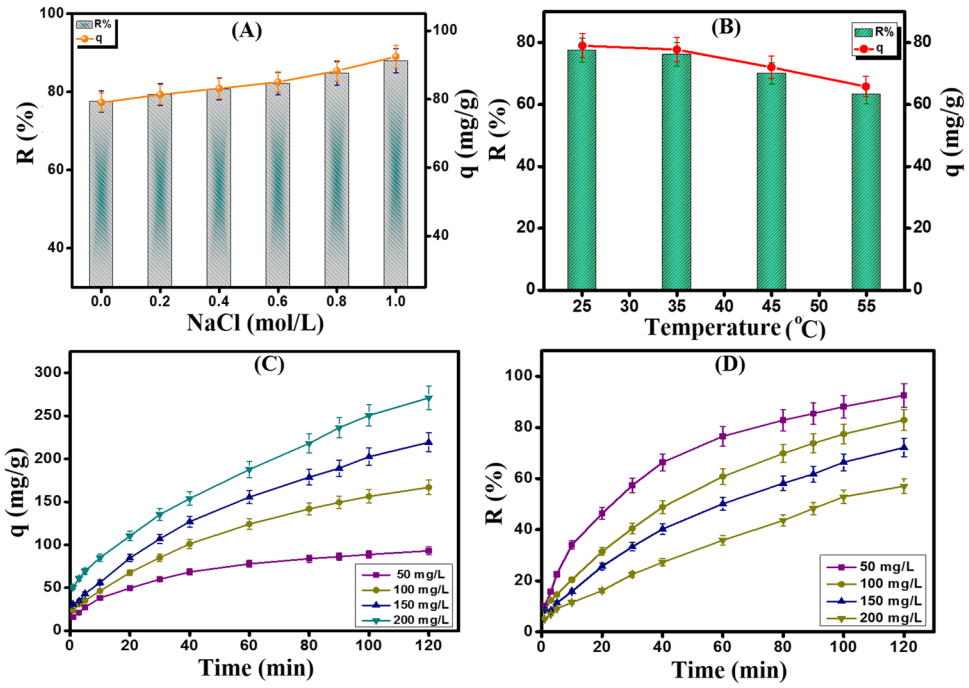

Fig. 6 **A** Effect of ionic strength [NaCl concentration = 0.2–1.0 mol/L, pH = 6, C_o = 50 mg/L, m = 0.01 g, and T = 25 °C], **B** effect of process temperature [T = 25–55 °C, pH = 6, C_o = 50 mg/L, and m = 0.01 g], and **C**, **D** effect of initial concentration of o-NP [C_o = 50–200 mg/L, T = 25 °C, pH = 6, and m = 0.01 g] on the adsorption of o-NP onto Fe_3O_4-κ-Carr/MIL-125(Ti) composite

The effect of the initial concentration

Figure 6C depicts the influence of the increment of the initial concentration of the bulk solution on the adsorption efficacy of o-NP. It was found that the increase in the o-NP concentration from 50 to 200 mg/g caused an increase in the adsorption capacity from 93.02 to 271.11 mg/g. This finding may be explained by the concentration increase in the bulk solution, generating strong driving forces of o-NP toward the Fe_3O_4-κ-Carr/MIL-125(Ti) surface. Thence, such potent forces could overcome the mass transfer resistance to the migration of o-NP from the bulk solution to Fe_3O_4-κ-Carr/MIL-125(Ti) surface (Gomaa et al. 2022a). On the contrary, this increase in the concentration of o-NP solution resulted in a diminution in the removal % from 92.54 to 57.05%, which is most likely due to the inadequate binding sites into the Fe_3O_4-κ-Carr/MIL-125(Ti) surface (Fig. 6D) (Eltaweil et al. 2022c). Overall, Fe_3O_4-κ-Carr/MIL-125(Ti) composite not only exhibited efficient adsorption performance toward the detrimental o-NP but also fast adsorption since the equilibrium time was 60 min.

Kinetic study

The experimental results pointed out that the adsorption of o-NP onto Fe_3O_4-κ-Carr/MIL-125(Ti) composite may occur via diverse mechanisms, depending on the heterogeneity of the binding sites onto the composite surface and physicochemical conditions. Therefore, various kinetic models: pseudo-first-order (PFO), pseudo-second-order (PSO), and Elovich, were utilized to analyze the resultant experimental data (Fig. 7A-C). The linear expressions of the applied models are listed in Table S2.

Table 1 The derived parameters from PFO, PSO, and Elovich kinetic models of the adsorption of o-NP onto Fe_3O_4-κ-Carr/MIL-125(Ti) composite

Kinetic models and parameters	Concentration (mg/L)			
	50	100	150	200
$q_{e,\,exp}$ (mg/g)	93.02	166.99	219.37	271.11
PFO				
$q_{e,cal}$ (mg/g)	65.37	104.58	134.29	172.74
k_1 (min^{-1})	0.046	0.039	0.036	0.031
R^2	0.989	0.977	0.979	0.975
PSO				
$q_{e,cal}$ (mg/g)	100.90	190.84	250.00	289.02
k_2 ($g.mg^{-1}.min^{-1}$)	0.0007	0.0004	0.0002	0.0001
R^2	0.997	0.987	0.983	0.985
Elovich				
α (mg/g min)	22.29	26.04	33.11	72.02
β (g/mg)	0.056	0.031	0.024	0.022
R^2	0.958	0.888	0.863	0.820

It was deduced from the computed R^2 values (Table 1) that PSO is more suitable than PFO to represent the o-NP adsorption onto Fe_3O_4-κ-Carr/MIL-125(Ti) composite since R^2-PSO > R^2-PFO (Eltaweil et al. 2022b). Furthermore, the obtained q_{cal} from PSO are closer to q_{exp} than those calculated from PFO. Besides, the favorability of

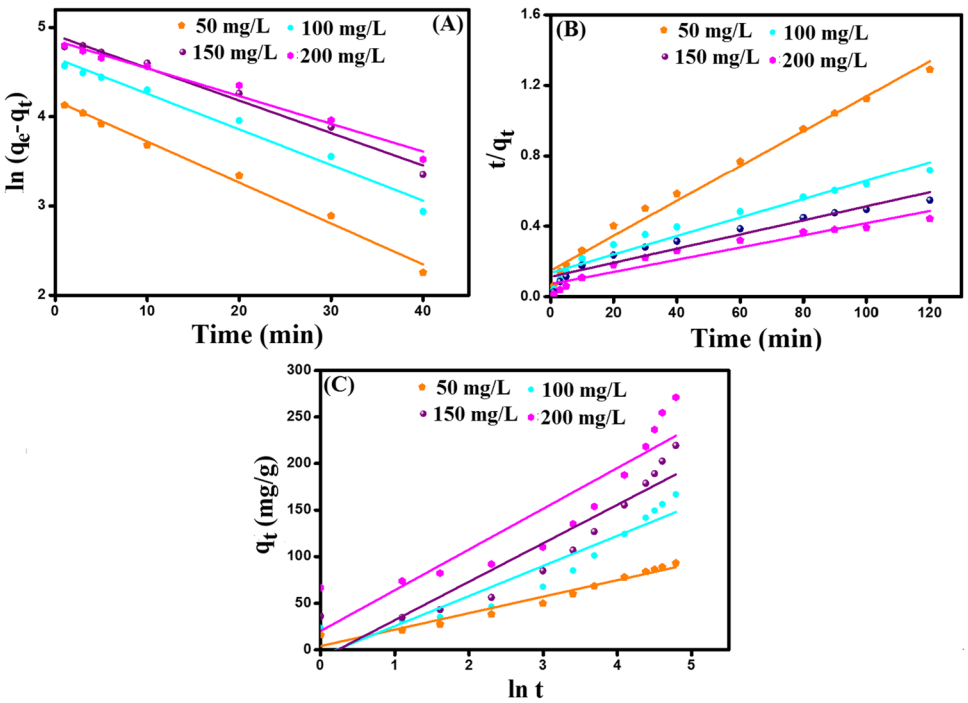

Fig. 7 Kinetic study **A** PFO, **B** PSO, and **C** Elovich models

the o-NP adsorption process was proved by Elovich model since the rate of o-NP adsorption onto Fe_3O_4-κ-Carr/MIL-125(Ti) was greater than the desorption rate.

Isotherm study

The type of interactions between o-NP and Fe_3O_4-κ-Carr/MIL-125(Ti) composite at equilibrium was scrutinized by bountiful isotherm models, including Langmuir, Freundlich, and Temkin (Fig. 8A–C). The linear expressions of these models were summarized in Table S3.

The obtained isotherm parameters (Table 2) point out that Freundlich model ($R^2 = 0.999$) is more fitted than Langmuir ($R^2 = 0.984$) and Temkin ($R^2 = 0.983$) to model the equilibrium data of the o-NP adsorption onto Fe_3O_4-κ-Carr/MIL-125(Ti). Additionally, the b value from Temkin model evinced the same result since $b < 80$ kJ/mol. Moreover, it was found that $n > 2$ reflects the favorability of the o-NP adsorption process onto Fe_3O_4-κ-Carr/MIL-125(Ti) composite. Furthermore, the calculated q_{max} of o-NP onto Fe_3O_4-κ-Carr/MIL-125(Ti) composite under Langmuir was 320.26 mg/g at pH 6 and 25 °C.

Reusability study

It is apparent from the recyclability test (Fig. 8D) that Fe_3O_4-κ-Carr/MIL-125(Ti) composite has remarkable recyclability where its adsorption performance toward o-NP was still high after the 5th cycle ($q = 58.94$ mg/g and $R\% = 56.01\%$). This finding confirmed the significance of these magnetic adsorbents that provide a fast, easy, and impeccable separation after the adsorption processes using an external magnet.

Table 2 The parameters derived from Langmuir, Freundlich, and Temkin isotherm models for the adsorption of o-NP onto Fe_3O_4-κ-Carr/MIL-125(Ti) composite

Isotherm model	Parameter	Value
Langmuir	q_m (mg/g)	320.26
	b (L/mg)	0.027
	R^2	0.984
Freundlich	n	2.77
	k_F (L/mg)	14.18
	R^2	0.999
Temkin	A (L/g)	0.489
	B (J/mol)	44.36
	b (KJ/mol)	0.051
	R^2	0.983

The proposed adsorption mechanism

Understanding the adsorption mechanism is a quintessential point in any adsorption process, so the controlled mechanism on the adsorption of o-NP onto Fe_3O_4-κ-Carr/MIL-125(Ti) composite was studied based on XPS analysis, ZP measurements, and the experimental results. XPS survey of Fe_3O_4-κ-Carr/MIL-125(Ti) after the adsorption of o-NP (Fig. 9A) showed the characteristic peak of N1s, evincing the adsorption of o-NP. The presence of o-NP in the molecular

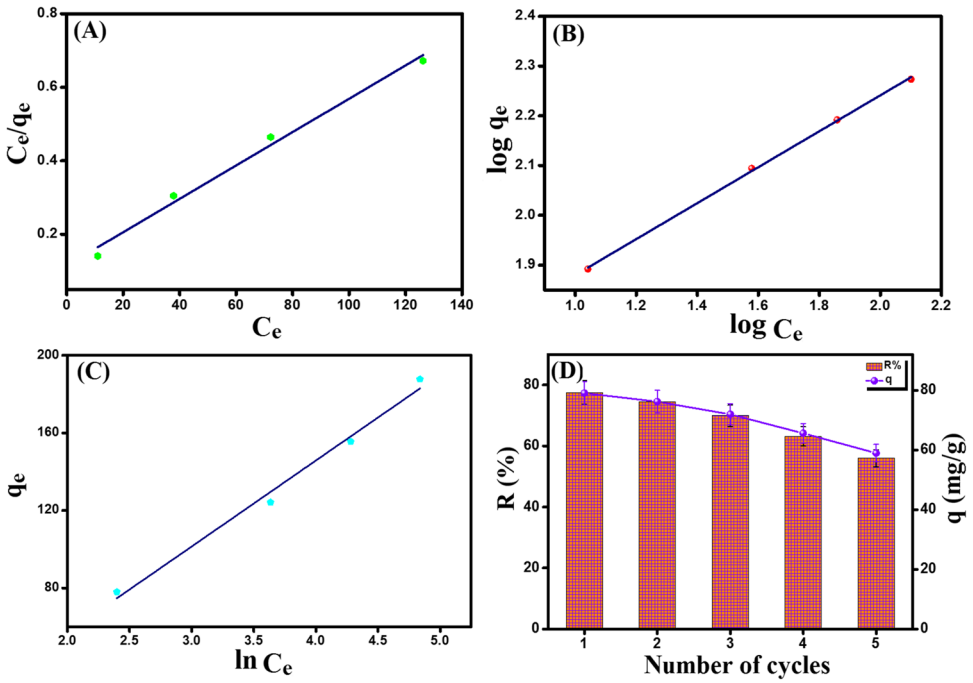

Fig. 8 Isotherm study. **A** Langmuir, **B** Freundlich, and **C** Temkin models, and **D** recyclability test [NaOH concentration = 1 M, pH = 6, $C_o = 50$ mg/L, $m = 0.01$ g, and $T = 25$ °C]

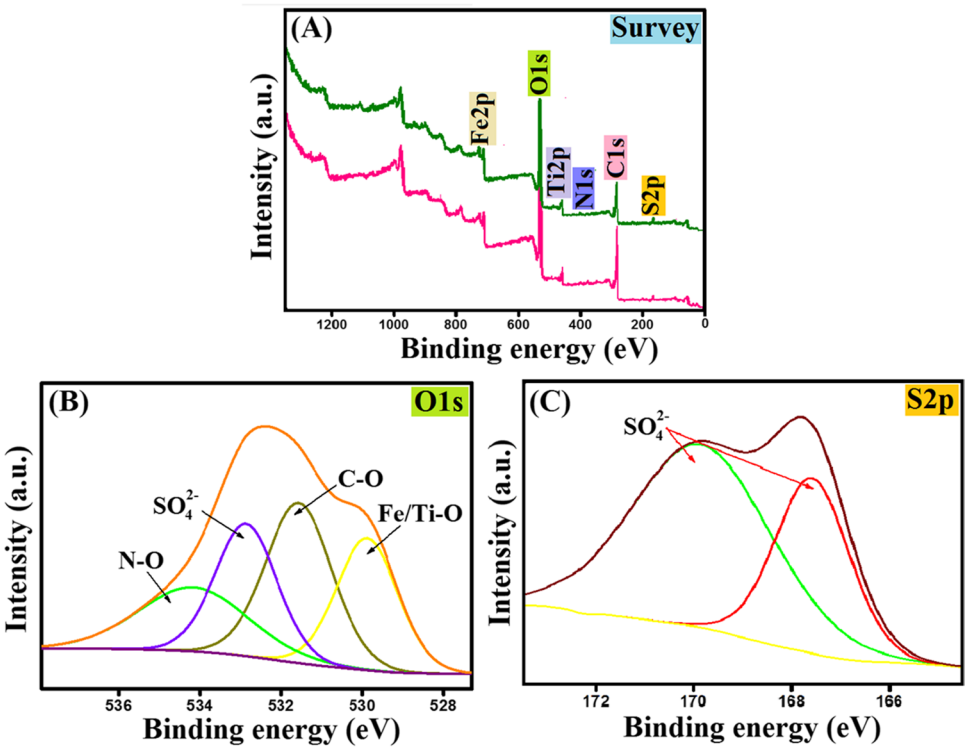

Fig. 9 XPS spectra of Fe_3O_4-κ-Carr/MIL-125(Ti); **A** survey before and after the adsorption of o-NP, **B** O1s, and **C** S2p after the adsorption process

form at pH < 7.23 suggested that the electrostatic interaction is not the dominant mechanism, and other physical and chemical interactions that played positive and negative effects on the o-NP adsorption process, including (i) H-bonding between the N and O-containing groups on the o-NP and the H-atoms of Fe_3O_4-κ-Carr/MIL-125(Ti) as well as the plentiful O-containing groups onto the Fe_3O_4-κ-Carr/MIL-125(Ti) surface and the H-atoms of o-NP; (ii) π-π interaction between the aromatic ring of BDC in the composite and the benzene ring in o-NP; (iii) electron donor–acceptor interaction between the e-donor groups in Fe_3O_4-κ-Carr/MIL-125(Ti) composite (OH, SO_4^{2-} and benzene ring) and the e-withdrawing group in o-NP (NO_2) as well as the e-withdrawing group in the composite (COOH) and the e-donor groups in o-NP (OH and benzene ring). The occurrence of these physicochemical interactions between o-NP and Fe_3O_4-κ-Carr/MIL-125(Ti) was confirmed by the peak shift of the XPS spectra of O1s and S2p after the o-NP adsorption (Fig. 9B, C). (iv) The electrostatic repulsion forces between the anionic o-NP and the negatively charged composite as clarified from ZP measurements in an alkaline medium, played a secondary negative role on the adsorption aptitude of o-NP.

Conclusion

This study reported the construction, characterization, and adsorbability evaluation of a new Fe_3O_4-κ-Carr/MIL-125(Ti) composite for removing the organic o-NP pollutant. The characterization stage inferred the successful formulation of the composite adsorbent. Surprisingly, increasing MIL-125(Ti) ratio three times than κ-Carr significantly boosted the removal (%) of o-NP from 60.99 to 77.55%, and the maximal adsorption capacity of o-NP attained 320.26 mg/g at pH 6 and 25 °C. Moreover, data obtained from kinetics and isotherm studies were fitted to Freundlich model and followed the pseudo-second-order model. The reusability test attested the potential capability of Fe_3O_4-κ-Carr/MIL-125(Ti) composite to adsorb o-NP after five repeated cycles with removal (%) exceeded 60%. Overall, the higher adsorption performance, facile separation, and recyclability features nominate the potential use of the formulated composite as an efficient adsorbent candidate for advanced water treatment.

Supplementary Information The online version contains supplementary material available at https://doi.org/10.1007/s11356-023-25678-2.

Acknowledgements We want to thank the editor and anonymous reviewers for their valuable comments and suggestions for this paper.

Author contribution Eman Abd El-Monaem, Abdelazeem Eltaweil, and Ahmed M. Omer: conceptualization, methodology, writing (review), formal analysis, and editing. Gehan M. El-Subruiti and Mohy-Eldin: review, editing, and supervision.

Funding Open access funding provided by The Science, Technology & Innovation Funding Authority (STDF) in cooperation with The Egyptian Knowledge Bank (EKB).

Data availability The datasets used and analyzed during the current study are available from the corresponding author on reasonable request.

Declarations

Ethics approval Not applicable.

Consent to participate Not applicable.

Consent for publication Not applicable.

Competing interests The authors declare no competing interests.

References

Abd El-Monaem EM, Omer AM, Khalifa RE, Eltaweil AS (2022) Floatable cellulose acetate beads embedded with flower-like zwitterionic binary MOF/PDA for efficient removal of tetracycline. J Colloid Interface Sci 620:333–345

Abdelfatah AM, Fawzy M, El-Khouly ME, Eltaweil AS (2021a) Efficient adsorptive removal of tetracycline from aqueous solution using phytosynthesized nano-zero valent iron. J Saudi Chem Soc 25:101365

Abdelfatah AM, Fawzy M, Eltaweil AS, El-Khouly ME (2021b) Green synthesis of nano-zero-valent iron using ricinus communis seeds extract: characterization and application in the treatment of methylene blue-polluted water. ACS Omega 6:25397–25411

Abdelfatah AM, El-Maghrabi N, Mahmoud AED, Fawzy M (2022) Synergetic effect of green synthesized reduced graphene oxide and nano-zero valent iron composite for the removal of doxycycline antibiotic from water. Sci Rep 12:1–19

Ammar C, Alminderej FM, El-Ghoul Y, Jabli M, Shafiquzzaman M (2021) Preparation and characterization of a new polymeric multilayered material based K-carrageenan and alginate for efficient bio-sorption of methylene blue dye. Polymers 13:411

Arof A, Shuhaimi N, Alias N, Kufian M, Majid S (2010) Application of chitosan/iota-carrageenan polymer electrolytes in electrical double layer capacitor (EDLC). J Solid State Electrochem 14:2145–2152

Attia NF, Abd El-Monaem EM, El-Aqapa HG, Elashery SE, Eltaweil AS, El Kady M, Khalifa SA, Hawash HB, El-Seedi HR (2022) Iron oxide nanoparticles and their pharmaceutical applications. Appl Surface Sci Adv 11:100284

Benmaati A, Boukoussa B, Hadjadj Aoul R, Hachemaoui M, Kerbadou RM, Habib Zahmani H, Hacini S (2022) Insights into catalytic reduction of organic pollutants catalyzed by nanoparticles supported on zeolite clinoptilolite. Silicon 14:8831–8843. https://doi.org/10.1007/s12633-022-01671-1

Chen J, Sun X, Lin L, Dong X, He Y (2017) Adsorption removal of o-nitrophenol and p-nitrophenol from wastewater by metal–organic framework Cr-BDC. Chin J Chem Eng 25:775–781

Cheng S, Liu Y, Xing B, Qin X, Zhang C, Xia H (2021) Lead and cadmium clean removal from wastewater by sustainable biochar derived from poplar saw dust. J Clean Prod 314:128074

Cheng S, Zhao S, Guo H, Xing B, Liu Y, Zhang C, Ma M (2022) High-efficiency removal of lead/cadmium from wastewater by MgO modified biochar derived from crofton weed. Biores Technol 343:126081

Das P, Debnath P, Debnath A (2021) Enhanced sono-assisted adsorptive uptake of malachite green dye onto magnesium ferrite nanoparticles: kinetic, isotherm and cost analysis. Environ Nanotechnol Monit Manag 16:100506

Deb A, Debnath A, Saha B (2021) Sono-assisted enhanced adsorption of eriochrome Black-T dye onto a novel polymeric nanocomposite: kinetic, isotherm, and response surface methodology optimization. J Dispersion Sci Technol 42:1579–1592

Duman O, Tunç S, Polat TG, Bozoğlan BK (2016) Synthesis of magnetic oxidized multiwalled carbon nanotube-κ-carrageenan-Fe3O4 nanocomposite adsorbent and its application in cationic Methylene Blue dye adsorption. Carbohyd Polym 147:79–88

Duman O, Özcan C, Polat TG, Tunç S (2019) Carbon nanotube-based magnetic and non-magnetic adsorbents for the high-efficiency removal of diquat dibromide herbicide from water: OMWCNT, OMWCNT-Fe3O4 and OMWCNT-κ-carrageenan-Fe3O4 nanocomposites. Environ Pollut 244:723–732

Eltaweil AS, El-Monaem EMA, Mohy-Eldin MS, Omer AM (2021) Fabrication of attapulgite/magnetic aminated chitosan composite as efficient and reusable adsorbent for Cr (VI) ions. Sci Rep 11:1–15

Eltaweil AS, Abdelfatah AM, Hosny M, Fawzy M (2022a) Novel biogenic synthesis of a Ag@ Biochar nanocomposite as an antimicrobial agent and photocatalyst for methylene blue degradation. ACS Omega 7:8046–8059

Eltaweil AS, El-Monaem A, Eman M, El-Subruiti GM, Ali BM, El-Latif A, Mona M, Omer AM (2022b) Graphene oxide incorporated cellulose acetate beads for efficient removal of methylene blue dye; isotherms, kinetic, mechanism and co-existing ions studies. J Porous Mater 1–12. https://doi.org/10.1007/s10934-022-01347-6

Eltaweil AS, Hashem OA, Abdel-Hamid H, Abd El-Monaem EM, Ayoup MS (2022c) Synthesis of a new magnetic sulfacetamide-ethylacetoacetate hydrazone-chitosan Schiff-base for Cr (VI) removal. Int J Biol Macromol 222:1465–1475

Ewis D, Ba-Abbad MM, Benamor A, Mahmud N, Nasser M, El-Naas M, Mohammad AW (2022) Adsorption of 4-nitrophenol onto iron oxide bentonite nanocomposite: process optimization, kinetics, isotherms and mechanism. Int J Environ Res 16:1–13

Fatima R, Park S, Kim J-O (2020) Effect of molar ration of Ti/Ligand on the synthesis of MIL-125 (Ti) and its adsorption and photocatalytic properties. J Ind Eng Chem 90:166–177

Gomaa H, El-Monaem A, Eman M, Eltaweil AS, Omer AM (2022a) Efficient removal of noxious methylene blue and crystal violet dyes at neutral conditions by reusable montmorillonite/NiFe2O4@ amine-functionalized chitosan composite. Sci Rep 12:1–16

Gomaa H, Hussein MA, Motawea MM, Aboraia AM, Cheira MF, Alotaibi MT, El-Bahy SM, Ali HM (2022b) A hybrid mesoporous CuO@ barley straw-derived SiO2 nanocomposite for adsorption and photocatalytic degradation of methylene blue from real wastewater. Colloids Surf, A 644:128811

Huang L, Jin S, Bao F, Tang S, Yang J, Peng K, Chen Y (2022) Construction of a physically cross-linked carrageenan/chitosan/calcium ion double-network hydrogel for 3-nitro-1, 2, 4-triazole-5-one removal. J Hazard Mater 424:127510

Jiang Q, Han Z, Yu X, Yuan Y, Ren Y, Li J, Zhao C, Cheng Z (2021) NH2-MIL-125 (Ti)/biochar fibers for enhanced direct dyes adsorption. J Environ Chem Eng 9:106636

Jin D, Xu Q, Yu L, Hu X (2015) Photoelectrochemical detection of the herbicide clethodim by using the modified metal-organic framework amino-MIL-125 (Ti)/TiO2. Microchim Acta 182:1885–1892

Karim MR, Aijaz MO, Alharth NH, Alharbi HF, Al-Mubaddel FS, Awual MR (2019) Composite nanofibers membranes of poly (vinyl alcohol)/chitosan for selective lead (II) and cadmium (II) ions removal from wastewater. Ecotoxicol Environ Saf 169:479–486

Kassem KO, Hussein MA, Motawea MM, Gomaa H, Alrowaili Z, Ezzeldien M (2021) Design of mesoporous ZnO@ silica fume-derived SiO2 nanocomposite as photocatalyst for efficient crystal violet removal: effective route to recycle industrial waste. J Clean Prod 326:129416

Khoshkho SM, Tanhaei B, Ayati A, Kazemi M (2021) Preparation and characterization of ionic and non-ionic surfactants impregnated κ-carrageenan hydrogel beads for investigation of the adsorptive mechanism of cationic dye to develop for biomedical applications. J Mol Liq 324:115118

Klongklaew P, Bunkoed O (2021) The enrichment and extraction of parabens with polydopamine-coated microporous carrageenan hydrogel beads incorporating a hierarchical composite of metal-organic frameworks and magnetite nanoparticles. Microchem J 165:106103

Lapwanit S, Sooksimuang T, Trakulsujaritchok T (2018) Adsorptive removal of cationic methylene blue dye by kappa-carrageenan/poly (glycidyl methacrylate) hydrogel beads: preparation and characterization. J Environ Chem Eng 6:6221–6230

Lazaro IA, Forgan RS (2019) Application of zirconium MOFs in drug delivery and biomedicine. Coord Chem Rev 380:230–259

Li L, Zhao J, Sun Y, Yu F, Ma J (2019) Ionically cross-linked sodium alginate/κ-carrageenan double-network gel beads with low-swelling, enhanced mechanical properties, and excellent adsorption performance. Chem Eng J 372:1091–1103

Li Y, Zhou M, Waterhouse GI, Sun J, Shi W, Ai S (2021) Efficient removal of cadmium ions from water by adsorption on a magnetic carbon aerogel. Environ Sci Pollut Res 28:5149–5157

Liang X-X, Wang N, Qu Y-L, Yang L-Y, Wang Y-G, Ouyang X-K (2018) Facile preparation of metal-organic framework (MIL-125)/chitosan beads for adsorption of Pb (II) from aqueous solutions. Molecules 23:1524

Liu L, Deng G, Shi X (2020) Adsorption characteristics and mechanism of p-nitrophenol by pine sawdust biochar samples produced at different pyrolysis temperatures. Sci Rep 10:1–11

Liu Z, Wang C, Wu Y, Geng L, Zhang X, Zhang D, Hu H, Zhang Y, Li X, Liu W (2021) Synthesis of uniform-sized and microporous MIL-125 (Ti) to boost arsenic removal by chemical adsorption. Polyhedron 196:114980

Loh K-S, Lee YH, Musa A, Salmah AA, Zamri I (2008) Use of Fe3O4 nanoparticles for enhancement of biosensor response to the herbicide 2, 4-dichlorophenoxyacetic acid. Sensors 8:5775–5791

Ma H, Xu Z, Wang W, Gao X, Ma H (2019) Adsorption and regeneration of leaf-based biochar for p-nitrophenol adsorption from aqueous solution. RSC Adv 9:39282–39293

Marques BS, Dalmagro K, Moreira KS, Oliveira ML, Jahn SL, De Lima Burgo TA, Dotto GL (2020) CaeAl, NieAl and ZneAl LDH powders as efficient materials to treat synthetic effluents containing o-nitrophenol. J Alloys Compd 838:155628. https://doi.org/10.1016/j.jallcom.2020.155628

Mittal H, Al Alili A, Alhassan SM (2020) High efficiency removal of methylene blue dye using κ-carrageenan-poly (acrylamide-co-methacrylic acid)/AQSOA-Z05 zeolite hydrogel composites. Cellulose 27:8269–8285

Mokhtar A, Abdelkrim S, Djelad A, Sardi A, Boukoussa B, Sassi M, Bengueddach A (2020) Adsorption behavior of cationic and anionic dyes on magadiite-chitosan composite beads. Carbohyd Polym 229:115399

Moreira MA, Santos MP, Silva CG, Loureiro JM, Chang J-S, Serre C, Ferreira AF, Rodrigues AE (2018) Adsorption equilibrium of xylene isomers and ethylbenzene on MIL-125 (Ti) _NH2: the temperature influence on the para-selectivity. Adsorption 24:715–724

Omer AM, El-Monaem A, Eman M, El-Subruiti GM, El-Latif A, Mona M, Eltaweil AS (2021) Fabrication of easy separable and reusable MIL-125 (Ti)/MIL-53 (Fe) binary MOF/CNT/Alginate composite microbeads for tetracycline removal from water bodies. Sci Rep 11:1–14

Priyadarshi G, Raval NP, Trivedi MH (2022) Microwave-assisted synthesis of cross-linked chitosan-metal oxide nanocomposite for methyl orange dye removal from unary and complex effluent matrices. Int J Biol Macromol 219:53–67

Raval NP, Mukherjee S, Shah NK, Gikas P, Kumar M (2021) Hexametaphosphate cross-linked chitosan beads for the eco-efficient removal of organic dyes: tackling water quality. J Environ Manage 280:111680

Rhim J-W, Wang L-F (2014) Preparation and characterization of carrageenan-based nanocomposite films reinforced with clay mineral and silver nanoparticles. Appl Clay Sci 97:174–181

Rice EW, Baird RB, Eaton AD, Clesceri LS (eds) (2012) Standard methods for the examination of water and wastewater, vol. 10. American Public Health Association, Washington, DC

Sadoon ZA, M-Ridha MJ (2019) Optimization of the electro coagulation process for the removal of cadmium from aqueous solution using RSM. Assoc Arab Univ J Eng Sci 26(4):52–64

Saha B, Debnath A, Saha B (2022) Fabrication of PANI@ Fe–Mn–Zr hybrid material and assessments in sono-assisted adsorption of methyl red dye: uptake performance and response surface optimization. J Indian Chem Soc 99:100635

Sharma S, Sharma G, Kumar A, Algarni TS, Naushad M, Alothman ZA, Stadler FJ (2022) Adsorption of cationic dyes onto carrageenan and itaconic acid-based superabsorbent hydrogel: synthesis, characterization and isotherm analysis. J Hazard Mater 421:126729

Shen M, Zhang Y, Xu H, Ma H (2021) MOFs based on the application and challenges of perovskite solar cells. Iscience 24:103069

Toto NA, Elhenawy HI, Eltaweil AS, El-Ashram S, El-Samad LM, Moussian B, El Wakil A (2022) Musca domestica (Diptera: Muscidae) as a biological model for the assessment of magnetite nanoparticles toxicity. Sci Total Environ 806:151483

Tran TK, Kim N, Le QC, Nguyen MT, Leu HJ, Thi KNV (2021) Electrochemical preparation and characterization of polyaniline enhanced electrodes: an application for the removal of cadmium metals in industrial wastewater. Mater Chem Phys 261:124221

Wu J, Wang T, Wang J, Zhang Y, Pan W-P (2021) A novel modified method for the efficient removal of Pb and Cd from wastewater by biochar: enhanced the ion exchange and precipitation capacity. Sci Total Environ 754:142150

Xu Y, Rashwan AK, Osman AI, El-Monaem A, Eman M, Elgarahy AM, Eltaweil AS, Omar M, Li Y, Mehanni A-HE (2022) Synthesis and potential applications of cyclodextrin-based metal–organic frameworks: a review. Environ Chem Lett. https://doi.org/10.1007/s10311-022-01509-7

Yang M, Wang M (2018) Adsorption of p-nitrophenol onto partially reduced graphene oxide: an experimental and theoretical study. Prog React Kinet Mech 43:189–200

Yang Z, Ding J, Feng J, He C, Li Y, Tong X, Niu X, Zhang H (2018) Preparation of BiVO4/MIL-125 (Ti) composite with enhanced visible-light photocatalytic activity for dye degradation. Appl Organomet Chem 32:e4285

Yu F, Cui T, Yang C, Dai X, Ma J (2019) κ-Carrageenan/sodium alginate double-network hydrogel with enhanced mechanical properties, anti-swelling, and adsorption capacity. Chemosphere 237:124417

Zhao H, Song F, Su F, Shen Y, Li P (2021) Removal of cadmium from contaminated groundwater using a novel silicon/aluminum nanomaterial: an experimental study. Arch Environ Contam Toxicol 80:234–247